University of Glasgow

Miras, H. N. , Sartzi, H., Long, D.-L. , Sproules, S. and Cronin, L. (2018) Directed self-assembly, symmetry breaking, and electronic modulation of metal oxide clusters by pyramidal heteroanions. *Chemistry: A European Journal*, 24(17), pp. 4399-4411.

There may be differences between this version and the published version. You are advised to consult the publisher's version if you wish to cite from it.

Miras, H. N. , Sartzi, H., Long, D.-L. , Sproules, S. and Cronin, L. (2018) Directed self-assembly, symmetry breaking, and electronic modulation of metal oxide clusters by pyramidal heteroanions. *Chemistry: A European Journal*, 24(17), pp. 4399-4411. (doi:10.1002/chem.201705711)

This article may be used for non-commercial purposes in accordance with Wiley Terms and Conditions for Self-Archiving.

http://eprints.gla.ac.uk/155212/

Deposited on: 12 January 2018

# Directed Self-Assembly, Symmetry Breaking, and Electronic Modulation of Metal Oxide Clusters by Pyramidal Heteroanions

*Harikleia Sartzi, De-Liang Long, Stephen Sproules,* Leroy Cronin* and Haralampos N. Miras**

WestCHEM, School of Chemistry, University of Glasgow, University Avenue, Glasgow G12 8QQ, UK

E-mail: charalampos.moiras@glasgow.ac.uk

Electronic Supplementary Information (ESI) available: [details of any supplementary information available should be included here]. See DOI: 10.1039/x0xx00000x

**Abstract.** Mixed valence/metal polyoxometalate (POM) clusters are one of the most interesting host species showing the ability to incorporate a wide range of heteroatoms of various charges and geometries. We report herein, the incorporation of different pyramidal $EO_3^{2-}$ heteroanions (E = PH, S, Se, Te) which are responsible not only for directing the templated assembly of a family of mixed-metal POMs but also for the symmetry-breaking of the traditional Dawson architecture and modulation of the electronic characteristics of the cluster's shell. The isolated family of POMs consists of four members: $(Me_2NH_2)_5Na_2[Mo_{11}V_7O_{52}(HPO_3)]\cdot MeOH\cdot 5H_2O$ (**1**), $(NH_4)_7[Mo_{11}V_7O_{52}(SO_3)]\cdot 12H_2O$ (**2**), $K_7[Mo_{11}V_7O_{52}(SeO_3)]\cdot 31H_2O$ (**3**), $(Me_2NH_2)_6Na[Mo_{11}V_7O_{52}(TeO_3)]\cdot 15H_2O$ (**4**), and were characterized by X-ray structural analysis, electrospray ionization mass spectrometry (ESI-MS), thermogravimetric analysis (TGA), UV-vis, IR, elemental and flame atomic absorption spectroscopy (FAAS) analysis, and inductively coupled plasma optical emission spectroscopy (ICP-OES). Cyclic voltammetry (CV) and electron paramagnetic resonance (EPR) spectroscopic studies in concert with density functional theoretical (DFT) calculations elucidate the effect of the heteroatom on the electronic properties of the cluster.

## Introduction

Polyoxometalates (POMs) have attracted the attention of many research groups during the last 25 years due to their remarkable structural motifs, electronic properties[1] and also the potential application in scientific fields, such as energy storage,[2] magnetism,[3] catalysis,[4] and medicine.[5] POMs are constructed by W, Mo, V or Nb based metal centers in high oxidation states and synthesized in a "one-pot" process. The associated self-assembly involves the condensation of $MO_x$ units to a final composition and topology that is dictated by a long list of experimental variables, such as pH, ionic strength, counter ions, and temperature. Alternatively heteropolyoxometalates, such as the widely investigated Wells-Dawson type $[M_{18}O_{54}(EO_4)_2]^{z-}$ clusters, are mainly templated by tetrahedral heteroanions such as phosphates, sulfates or arsenates (E = P, S, As).[6] In addition there are several examples that incorporate heteroanions in unusual geometries, such as the 18-molybdopyrophosphate anion, $[Mo_{18}O_{54}(P_2O_7)]^{4-}$, templated by a di-tetrahedral anion with redox inert $P^V$ centers,[7] and the $[H_3W_{18}O_{56}(EO_6)]^{6-}$ anion, which consists of a Dawson-type $\{W_{18}O_{54}\}$ shell enclosing an octahedral (E = Te, I) moiety,[8,9] which promotes the template assisted assembly of the cluster and induces catalytic functionality. Heteropolyoxometalates incorporating one or two templating heteroatoms which adopt non-tetrahedral geometries are exceedingly rare. More specifically, the first examples of clusters incorporating pyramidal heteroanions are $Mo^V$– and $V^{IV}$–based sulfite species, such as $(NH_4)_{20}[Mo_{12}O_{24}(SO_3)_{16}]\cdot 4H_2O$ and $(NH_4)_{15}\{Na[Mo_6O_{15}(SO_3)_4]_2\}\cdot 15H_2O$,[10] the two electron reduced Dawson anion $(Et_3NH)_6[Mo_{18}O_{54}(SO_3)_2]\cdot 4H_2O$ with two templating sulfite ($SO_3^{2-}$) ions,[11] and the $[(V^{IV}O)_6(\mu_4\text{-}O)_2(\mu_3\text{-}OH)_2(\mu_3\text{-}SO_3)_4(H_2O)_2]^{2-}$ family.[12] The molybdenum-based moieties combined with the ability of the vanadium metal centers to adopt various oxidation states ($V^{III}$, $V^{IV}$, $V^V$) and coordination modes led to a remarkable structural diversity.[13-16]

The development of molecular metal oxide clusters offers a unique opportunity to generate complex building block libraries due to the stabilization of wide range of configurable subunits with different properties and organize them further into highly modular architectures. For example, the ability to construct core-shell molecular clusters allowed the control of compartmentalized reactions,[17] exploration of electron coupled structural reorganizations,[18] new type of oscillatory phenomena[19] as well as the development of nanocluster-based information storage devices.[20]

As has been described in the literature, the tungstate-based POM clusters incorporating non-classical heteroanions are less common due to the stability of their lacunary species.[9,17,21] On the other hand, more commonly mixed valence molybdenum/vanadium-based POMs templated by non-traditional heteroanions have been reported.[13-16] Thus, the rich redox chemistry of Mo and V based species coupled with the redox behavior of the $EO_3^{2-}$ anions offer a unique opportunity for the design of highly modular molecular species with desirable functionality.

Herein, we present the synthesis and characterization of two new mixed-metal (Mo/V) egg-shaped POMs: $(Me_2NH_2)_5Na_2[Mo_{11}V^{V}_5V^{IV}_2O_{52}(HPO_3)]\cdot MeOH\cdot 5H_2O$ (**1**) and $(Me_2NH_2)_6Na[Mo_{11}V^{V}_5V^{IV}_2O_{52}(TeO_3)]\cdot 15H_2O$ (**4**), encapsulating pyramidal heteroatoms, namely phosphite ($HPO_3^{2-}$) and tellurite ($TeO_3^{2-}$), respectively. The compounds were characterized in solid state by X-ray analysis, TGA, IR as well as in solution by electrospray ionization mass spectrometry (ESI-MS), UV-vis and cyclic voltammetry. These clusters are the newest additions to a family of Dawson-like POMs that began with the sulfite analogue, $(NH_4)_7[Mo_{11}V^{V}_5V^{IV}_2O_{52}(SO_3)]\cdot 12H_2O$ (**2**),[13] and subsequently the selenite variant, $K_7[Mo_{11}V^{V}_5V^{IV}_2O_{52}(SeO_3)]\cdot 31H_2O$ (**3**).[16] This detailed examination of this series reveals the nuanced modulation of the electronic properties of the cluster by the encapsulated heteroanion.

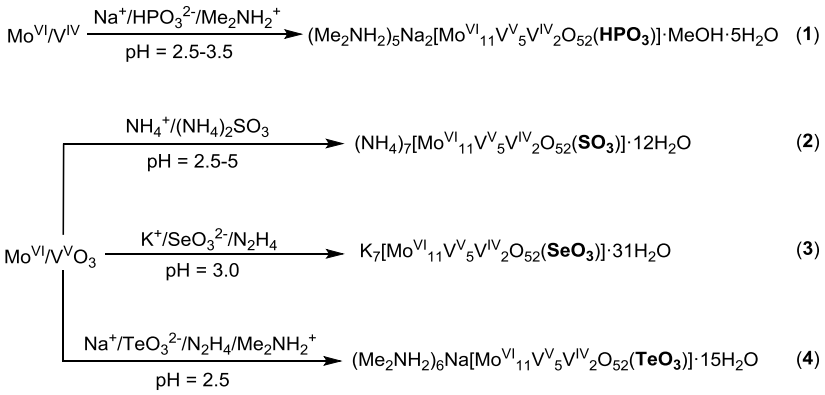


**Scheme 1.** Synthetic procedure of **1** – **4**

## Experimental Section

**Synthesis of Complexes.** The compounds $(NH_4)_7[Mo_{11}V_7O_{52}(SO_3)]\cdot 12H_2O$ (**2**) and $K_7[Mo_{11}V_7O_{52}(SeO_3)]\cdot 31H_2O$ (**3**) were prepared according to previously publised procedures.[13,16] The chemicals and solvents were purchase from Sigma-Aldrich and Alfa Aesar and used without further purification.

**$(Me_2NH_2)_5Na_2[Mo_{11}V_7O_{52}(HPO_3)]\cdot MeOH\cdot 5H_2O$ (1).** A mixture of $Na_2MoO_4\cdot 2H_2O$ (0.71 g, 2.93 mmol), $VOSO_4\cdot xH_2O$ (0.16 g, 0.98 mmol), $Na_2HPO_3\cdot 5H_2O$ (0.11 g, 0.51 mmol) and $Me_2NH\cdot HCl$ (0.25 g, 3.06 mmol) were dissolved in a warm mixture of deionized water (10 mL) and methanol (5 mL) under vigorous stirring, resulting in a dark purple solution. The mixture was left to cool down to room temperature under magnetic stirring and then the pH was adjusted carefully to 2.9 by the addition of concentrated HCl. At this point the solution turned dark green, and the reaction mixture was stirred for an additional 5 min. The dark green solution was filtered and the filtrate was left for 7 d after which dark green needles were collected by vacuum filtration and dried in air. Yield: 50 mg (30% based on V).

Anal. Calcd. for $C_{11}H_{55}Mo_{11}N_5O_{61}PNa_2V_7$: C, 4.85; H, 2.04; Mo, 38.77; N, 2.57; P, 1.14; Na, 1.69; V, 14.10. Found: C, 4.87; H, 2.85; Mo, 38.30; N, 2.42; P, 1.17; Na, 1.70; V, 14.40. IR (KBr, $cm^{-1}$): 3451 b, 3131 b, 1618 m, 1463 s, 1058 m, 951 s, 853 s, 805 s, 774 m, 583 s.

**$(Me_2NH_2)_6Na[Mo_{11}V_7O_{52}(TeO_3)]\cdot 15H_2O$ (4).** To a beaker charged with deionized water (20 mL) were added $Na_2MoO_4\cdot 2H_2O$ (2.00 g, 8.27 mmol), $NaVO_3$ (0.52 g, 4.26 mmol), $Na_2TeO_3$ (0.47 g, 2.12 mmol) and $Me_2NH\cdot HCl$ (2.00 g, 24.5 mmol), and the mixture vigorously stirred. Heating this turbid reaction mixture at 90 °C for 10 min gave a pale yellow solution. After cooling to room temperature, $N_2H_4\cdot 2HCl$ (0.07 g, 0.67 mmol) was added in a single portion producing a dark brown slurry. The mixture was stirred for 5 min before adjusting the pH to a value of 2.5 by addition of concentrated HCl. The resultant deep purple mixture was filtered, and the filtrate was layered with MeOH which after a week afforded diffraction-quality single crystals. Yield: 34 mg (7% based on V).
Anal. Calcd. for $C_{12}H_{78}Mo_{11}N_6O_{70}NaTeV_7$: C, 4.82; H, 2.63; Mo, 35.31; N, 2.81; Na, 0.77; Te, 4.27; V, 11.93. Found: C, 5.00; H, 2.91; Mo, 34.68; N, 2.69; Na, 0.79; Te, 4.19; V, 11.72. IR (KBr, $cm^{-1}$): 3433 b, 3168 b, 1626 m, 1464 s, 1015 m, 983 s, 847 s, 773 m, 669 m, 518 m.

**X-Ray Crystallographic Data Collection and Refinement of 1 and 4.** Suitable single crystal was selected and mounted onto a rubber loop using Fomblin oil. Single-crystal X-ray diffraction data of **1** and **4** were recorded on a Bruker Apex CCD diffractometer ($\lambda$ ($MoK_\alpha$) = 0.71073 Å) at 150 K equipped with a graphite monochromator. Structure solution and refinement were carried out with SHELXS-97[22] and SHELXL-97[23] using the WinGX software package.[24] Data collection and reduction were performed using the Apex2 software package. Corrections for incident and diffracted beam absorption effects were applied using empirical absorption corrections.[25] All the Mo and V atoms (including

those disordered) and most of the O atoms were refined anisotropically. Solvent water molecule sites with partial occupancy were found and included in the refinement of the structure. Crystallographic formulae typically contain a lot more water molecules in the crystal lattice than the formulae used for chemical analyses as samples were dried. Final unit cell data and refinement statistics for compounds **1** and **4** are collated in Table S1. The crystallographic data for compounds **1** and **4** (CCDC 1568505 and 1568506) can be obtained free of charge from the Cambridge Crystallographic Data Centre, 12, Union Road, Cambridge CB2 1EZ; fax:(+44) 1223- 336-033, deposit@ccdc.cam.ac.uk.

**Physical Measurements.** IR spectra were measured using JASCO FTIR 410 and Shimadzu FTIR 8400S spectrometers. UV-Vis spectra were obtained using a JASCO V-670 spectrophotometer. Thermogravimetric analysis was performed on a TA Instruments Q 500 thermogravimetric analyzer under nitrogen flow at a typical heating rate of 10 °C $min^{-1}$ in a platinum pan. Cyclic voltametry (CV) was performed using CHI 760D bi-potentiostat. The standard three-electrode arrangement was employed with a Pt mesh as auxiliary electrode, glassy carbon working electrode, and Ag/AgCl reference electrode. All potentials are quoted relative to the Ag/AgCl reference electrode. The glassy carbon working electrodes (diameter 1.5 mm) were polished with alumina (3 $\mu$m) on polishing pads, rinsed with distilled water, sonicated in $H_2O$ and then acetone before each experiment. The cell was purged with Ar for 10 min before each experiment. All experiments were performed at room temperature, and a scan rate of 50–400 mV $s^{-1}$. The supporting electrolyte was 0.1 M HOAc/NaOAc buffer solution (2.4 mL of 0.1 M NaOAc solution and 7.6 mL of a 0.1 M HOAc solution) containing 0.2 M (284 mg) $Na_2SO_4$. Finally 80 mg of each compound added to the above solution. Electrospray ionisation mass spectrometry (ESI-MS) was performed using a Bruker micrOTOF-Q quadrupole time-of-flight mass spectrometer. Samples were dissolved in water and acetonitrile introduced into the mass

spectrometer at a dry gas temperature of 180 °C. The ion polarity for all scans recorded was negative, with the voltage of the capillary tip set at 4500 V, end plate offset at -500 V, funnel 1 RF at 400 Vpp and funnel 2 RF at 400 Vpp, hexapole RF at 200 Vpp, ion energy 5.0 eV, collision energy at 15 eV, collision cell RF at 2100 Vpp, transfer time at 120.0 $\mu$s, and the pre-pulse storage time at 20.0 $\mu$s and analysed using the Bruker Daltonics v4.1 software. $^{1}$H NMR spectra were recorded in DMSO-$d_6$ solutions using a Bruker AVI 400MHz NMR spectrometer. X-band EPR spectra were recorded on a Bruker ELEXSYS E500 spectrometer and simulations performed using Easyspin.[26] Elemental analyses were determined by the in-house microanalysis services using an EA 1110 CHNS, CE-440 Elemental Analyzer. Flame atomic absorption spectroscopy (FAAS) analysis was performed witha Perkin-Elmer 1100B atomic absorption spectrophotometer and ICP-OES.

**Calculations.** All calculations in this work were performed with the electronic structure program ORCA.[27] Geometry optimizations and numerical frequencies were carried out using the BP86 functional.[28] A segmented all-electron relativistically contracted (SARC) basis set of triple-ζ-quality (def2-TZVP) was used for metal atoms.[29] Core electrons were kept frozen and described by single Slater functions (core shells: O, 1s; P, S and V, 1s2p; Se, 1s3p; Mo, 1s3d; Te 1s4p). A scalar relativistic correction was applied using the zeroth-order regular approximation (ZORA) method.[30] An all-electron polarized triple-ζ-quality (def2-TZVP) basis set of the Ahlrichs' group was used for the other atoms.[31] Auxiliary basis sets for all complexes used to expand the electron density in the calculations were chosen to match the orbital basis. The conductor like screening model (COSMO)[32] was used for all calculations to account for solvent effects (water, ε = 80.4) which was used in electrochemical measurements. The solvent cavity around the surrounding the compounds was generated with a solvent-excluding surface based on the ionic radii of the surface atoms defined as 0.68 Å for vanadium,

0.72 Å for molybdenum and 1.52 Å for oxygen. A spin-unrestricted formulism was applied to all species. The self-consistent field (SCF) calculations were tightly converged ($1 \times 10^{-8}$ $E_h$ in energy, $1 \times 10^{-7}$ $E_h$ in the density change, and $1 \times 10^{-7}$ in the maximum element of the DIIS[33] error vector). The geometry search for all complexes was carried out in redundant internal coordinates without imposing geometry constraints. Canonical orbitals and spin density plots were constructed using the program Molekel.[34]

## Results and Discussion

**Synthesis.** Compounds **2** and **3** have been synthesized according to the previously reported methodology.[13,16] The general synthetic procedure for the preparation of these clusters involves the combination of the appropriate vanadate and molybdate salts with the heteroatom oxyanion (Figure 1). More specifically, deep green crystals of **2** were retrieved from the reaction mixture prepared by the sequential addition of $NH_4VO_3$ and $(NH_4)_2SO_3$ to an acidified aqueous solution containing $(NH_4)_6Mo_7O_{24}\cdot 4H_2O$. In a similar fashion, the addition of $KVO_3$, $K_2SeO_3$ and $N_2H_4\cdot 2HCl$ to an aqueous solution of $K_2MoO_4$, yielded a dark brown solution. Acidification of the reaction mixture to pH 3 using concentrated HCl led to the formation of brown hexagonal crystals of **3** within a week. In an extension of this reported work, we succeeded in completing the series of metal oxide clusters templated by $EO_3^{2-}$ anions by isolating two isostructural Dawson-like structures containing phosphite ($HPO_3^{2-}$) and tellurite ($TeO_3^{2-}$) anions. Both compounds were synthesized under "one-pot" reaction conditions. Compound **1** was prepared by the sequential addition of $Na_2MoO_4\cdot 2H_2O$, $VOSO_4\cdot xH_2O$, $Na_2HPO_3\cdot 5H_2O$ and dimethylamine hydrochloride to a warm solvent mixture of $H_2O$ and MeOH. The dark purple reaction mixture was left to cool down to room temperature. Then the pH was adjusted to

2.9 by drop-wise addition of concentrated HCl resulting to a dark green solution which was left undisturbed for a week during which period of time dark green needles of $(Me_2NH_2)_5Na_2[Mo_{11}V_7O_{52}(HPO_3)]\cdot MeOH\cdot 5H_2O$ were formed. Compound **1** can be synthesized within the pH range of 2.5–3.5, although the highest yield and purity have been obtained at the pH range 2.8–3.0. Compound **4** was synthesized by the addition of $Na_2MoO_4\cdot 2H_2O$, $NaVO_3$, $Na_2TeO_3$ and dimethylamine hydrochloride in aqueous medium. Due to the limited solubility of the vanadate salt in water, the obtained cloudy yellow colored mixture was heated at 90 °C resulting in a clear yellow solution. The reaction mixture was left to cool down at room temperature under magnetic stirring, followed by the addition of solid $N_2H_4\cdot 2HCl$ triggering a color change of the reaction mixture to dark green. The pH of the reaction mixture was adjusted to 2.5 by drop-wise addition of concentrated HCl giving finally a dark purple solution. Vapor diffusion of MeOH into the reaction mixture led to the formation of dark green needles of **4** after one week.

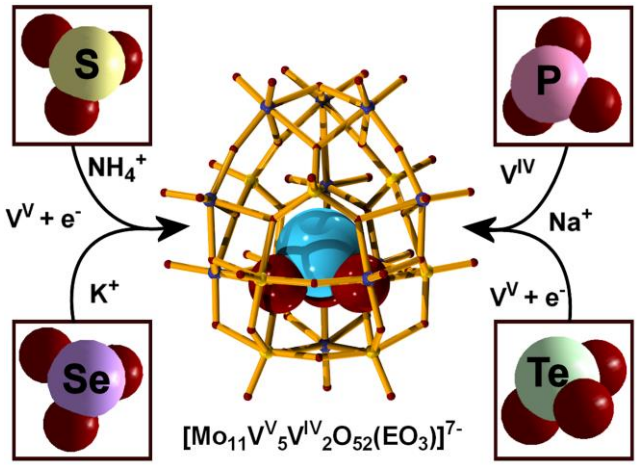


**Figure 1.** Ball and stick representation of the $[Mo_{11}V_7O_{52}(EO_3)]^{7-}$ clusters. In space-filling representation the four templating heteroanions $EO_3$ (E = PH, S, Se, Te) that have been trapped within the POM. Color code: Mo: dark blue, V: yellow, O: red, E: light blue (space filling representation).

It is worth noting a few important synthetic considerations which are crucial for the formation of these POMs. The synthesis of **2** and **3** involved the use of potassium- and ammonium-based salts followed by in situ reduction of the $V^{V}$ species, respectively. Any attempts to isolate **2** and **3** using sodium counterions were unsuccessful indicating that counterion effects are crucial for the stabilization of M/E-based (M = Mo, V; E = PH, S, Se, Te) building blocks which assemble into these egg-shaped clusters. Moreover, the synthesis of the **1** involved the use of a reduced vanadium source ($V^{IV}OSO_4{\cdot}xH_2O$) from the outset. Any effort to isolate **1** by partially reducing in situ the $V^{V}$ starting material were not successful leading to the formation of the common α-Keggin architecture templated by the $VO_4$ species. On the contrary, the use of vanadyl sulfate in the synthesis of **4** led to the formation of the previously reported "crowned" Dawson-like structure, $K_{10}[Mo^{VI}_{11}V^{V}_{5}V^{IV}_{2}O_{52}(Te^{VI}O_3)(Mo^{VI}_{6}V^{V}O_{22})]{\cdot}15H_2O$,[15] even after adjustment of the experimental conditions to a wide range of temperature, concentrations and pH values. Finally, the use of mixed solvent system ($H_2O$/MeOH) either during the reaction or during the crystallization is crucial for the formation of **1** and **4**. In the absence of methanol, the existing equilibria shifted towards the formation of previously reported species, such as α-Keggin and α-Dawson clusters. All the above observations demonstrate the existence of a complex network of equilibria between diverse building block libraries in the reaction mixtures. The pyramidal geometry of the heteroanion promotes the formation of diverse building blocks while their assembly can be additionally influenced by the lone pair of electrons and the atomic radius of the heteroanion in contrast to the traditional Mo/V archetypes previously reported.[35]

**Structural description of the compounds.** X-ray diffraction analyses revealed four isostructural Dawson-like mixed-metal (Mo/V) POMs of the general formula, $[Mo^{VI}_{11}V^{V}_{5}V^{IV}_{2}O_{52}(EO_3)]^{7-}$ where E

= PH **1**; S **2**; Se **3**; Te **4** (Figure 1). Each cluster consists of two hemispheres; the upper part is formed by three edge-sharing $MoO_6$ octahedra connected to the upper belt of the egg-shaped cluster through three $VO_4$ tetrahedra. The remaining four vanadium (2 $V^{V}$ and 2 $V^{IV}$) and five $Mo^{VI}$ centers are crystallographically disordered over the nine $MO_6$ octahedral positions of the lower hemisphere. According to bond valence sum (BVS) calculations on the upper hemisphere showed that the molybdenum centers are in the oxidation state +VI ($BVS_{av}$ = 6.05 **1** and 6.01 **4**) while the vanadium centers are in the oxidation state +V ($BVS_{av}$ = 5.09 **1** and 5.04 **4**). The oxidation state for the remaining four vanadium ions in the lower hemisphere cannot be assigned. The identification of the oxidation states of the remaining vanadium centers was made on basis of charge balance considerations of the entire compound, combined with BVS calculations[36] and elemental analyses, yielding an average BVS of 4.5 which is in good agreement with the theoretical experimental value ($BVS_{av}$ = 4.4) for two electrons shared between four positions. Delocalization of the two electrons within the lower hemisphere of the structure gives these clusters their dark green hue in the solution and solid state.

Finally the cavity of the lower hemisphere is occupied by a $HPO_3^{2-}$ in **1** and $TeO_3^{2-}$ in **4**, where the P and the Te atoms are in the oxidation states +III and +IV, respectively. The tetrahedral $VO_4$ centers located on the upper hemisphere of **1** are coordinated by three $\mu_3$-$O^{2-}$ moieties, with the V–O bonds in the range of 1.716(4) – 1.768(4) Å and one terminal oxo group with a V–O bond in the range of 1.614(4) – 1.627(5) Å. The Mo atoms in the same hemisphere exhibit two terminal oxo groups in *cis* position, with the terminal Mo–O group bond lengths in the range of 1.698(4) – 1.718(4) Å, one $\mu_2$-$O^{2-}$ and three $\mu_3$-$O^{2-}$ bridges with Mo–O bonds ranging 1.855(4) – 1.884(4) Å and 2.048(4) – 2.267(4) Å, respectively. Finally, in the case of **1**, a MeOH molecule found in the unit cell coordinated to a sodium counterion as a result of the crystallization method using a solvent mixture of $H_2O$/MeOH. Tellurite-containing **4** adopts a Dawson-like disordered architecture similar to the one observed in the case of the

sulfite- and selenite-templated clusters,[13,16] with the formula $[Mo^{VI}_{11}V^{VI}_{5}V^{IV}_{2}O_{52}(TeO_3)]^{7-}$ **4**, where its cavity is occupied by a tellurite ion. The main bond lengths in this case fall within a similar range; the tetrahedral $VO_4$ centers are coordinated by three $\mu_3$-$O^{2-}$ moieties, with the V–O bonds in the range of 1.727(9) – 1.777(6) Å and one terminal oxo bond distance ranging 1.60(1) – 1.615(7) Å. The Mo atoms in the same hemisphere possess two terminal oxo groups in the *cis* position, with the terminal Mo–O group bond lengths in the range of 1.697(7) – 1.708(7) Å, one $\mu_2$-$O^{2-}$ and three $\mu_3$-$O^{2-}$ bridges with Mo–O bonds between 1.876(7) – 1.896(7) Å and 1.889(7) – 2.044(9) Å, respectively. It is worth noting that no methanol co-crystallized with the POM even though the cluster can only be isolated in its presence. The structural features of the sulfite (**2**) and selenite (**3**) templated POMs have been described previously.[13,16]

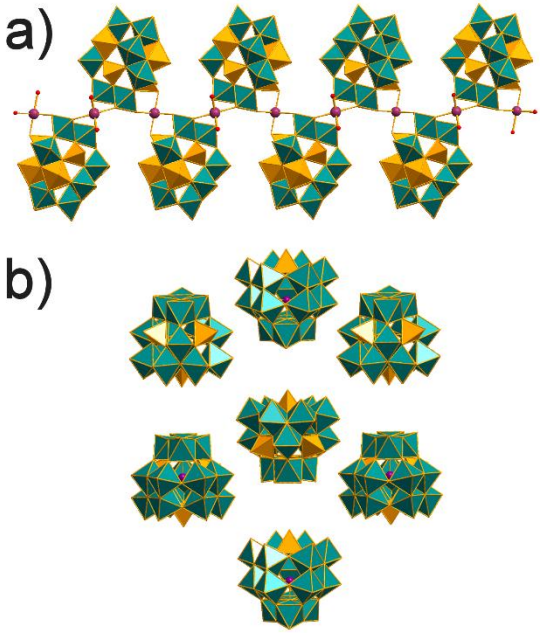


**Figure 2.** Polyhedral representation of the packing mode of compounds (a) **1** and (b) **4** along *b* axis. Color code: Mo, teal; V, light orange; Na: plum. Counterions have been omitted for clarity.

Additionally, the average P–O and S–O bond distance of the heteroanions in **1** and **2** were found to be similar 1.531(4) and 1.549(5) Å, respectively, with longer bonds for the Se- and Te-based POMs at 1.71(2) and 1.870(9) Å, respectively (Table S2). The elongation of the E–O bonds which was observed in every case due to the increased atomic radius of the heteroatom (S < P < Se < Te), is reflected to the smaller average O–E–O bond angle in the $EO_3^{2-}$ unit: **1**, 110.9(2)°; **2**, 103.6(3)°; **3**, 99.6(7)° and **4**, 95.2(4)° (Table S3). Additionally, the average distance of the heteroatom above the $O_3$ plane increases gradually from 0.479 to 0.652, 0.809 and 0.977 Å in **1** – **4**, respectively. Consequently, the heteroatom is located in each case further away from the plane defined by the six metal centers in the belt region of the lower hemisphere. All the above experimental observations are in excellent agreement with the ones predicted by our theoretical studies (vide infra). Utilization of different counterions resulted in the crystallization of all four compounds in different space groups and packing configurations (Figure 2). When sodium and dimethylammonium were employed, **1** crystallized in the $P\bar{1}$ space group, whereas **4** was in the *Pnma* space group. On the other hand, the presence of potassium counterions in the case of **2** and ammonium counterions in the case of **3** resulted in crystallization of the relevant species in the $P2_1/m$ and *P*-4*b*2 space groups.[13,16] Interestingly, the $EO_3^{2-}$ (E = PH, S, Se, Te) pyramidal anion directed the assembly of the Mo/V-based building blocks towards the formation of the $\{Mo_{11}V_7O_{52}\}$ shell accompanied by the "breaking" of the idealized symmetry from $D_{3h}$, $C_{3v}$ and $D_{3d}$ observed in the traditional Dawson architectures to $C_s$.[37] The generation of different isomers triggered by the assembly process ("assembly isomerism")[38] induces different local symmetry on the lower hemisphere of the POM. This is a key consideration in the interpretation of their EPR spectra (vide infra).

**Mass spectrometry.** In an effort to characterize further this family of clusters we employed high resolution electrospray ionization mass spectrometry (ESI-MS) to determine unambiguously the

structural integrity and composition of the POMs in solution. The composition as well as the structural integrity of the polyoxometalate anions of **1**, $[Mo_{11}V_7O_{52}(HPO_3)]^{7-}$, and **4**, $[Mo_{11}V_7O_{52}(TeO_3)]^{7-}$ in solution have been confirmed. The ESI-MS studies were performed in solvent mixture of $H_2O$/MeCN. The observation of a series of partially overlapping envelopes is due to the existence of multiple charged states of the same moiety, resulting from the variable number of protons and counterions, which consequently leads to the observation of overlapping isotopic distribution envelopes. This type of behavior is quite common in aqueous solution studies of POM compounds.[39] The overlapping distribution envelopes observed for **1** fall in the region of 1384.9 and 1478.9 *m*/*z* (Figure 3). These envelopes can be assigned to the general formulae $\{[Mo_{11}V_7O_{52}(HPO_3)]_m(MeOH)H_nNa_p(Me_2NH_2)_q(OH_2)_r\}^{z-}$, $m$ = 1 – 2, $n$ = 2 – 6, $p$ = 1 – 2, $q$ = 2 – 7, $r$ = 14 – 25, $z$ = 2 (Table S4). At higher *m*/*z* values it was possible to observe 3– charged supramolecular assemblies of the intact clusters in the region ca. 1600 – 2000 *m*/*z*. Similar behavior was observed in the case of **4** (Figure 4). The overlapped distribution envelopes observed in the range of 964.2 and 1640.4 *m*/*z* can be assigned to the above general formula with $m$ = 1 or 2, $n$ = 0 – 5, $p$ = 1 – 4, $q$ = 4 – 8, $r$ = 7 – 22, $z$ = 2 and 3 (Table S5). The change of the oxidation state of the metal centers is due to the ionization and consecutive ion-transfer process of the charged species and has been observed previously in numerous occasions.[13-18]

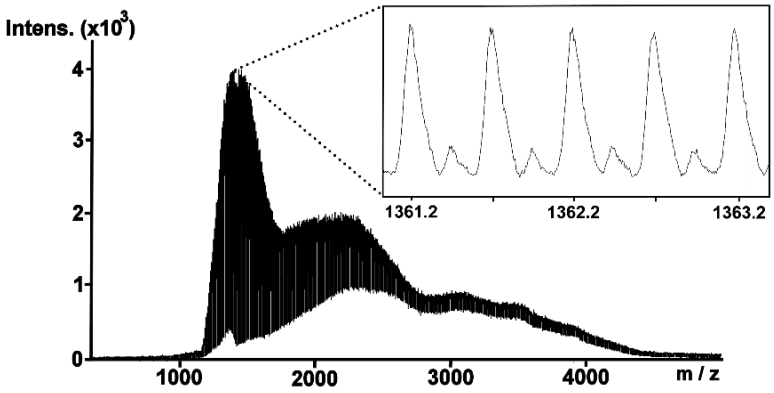

**Figure 3.** Negative ion mass spectrum of **1** in $H_2O$/MeCN. Inset: expanded distribution envelope of the discrete $\{Mo_{11}V_7O_{52}(HPO_3)\}$ POM. The peak separation of the distribution envelope reveals a doubly charged ($z = -2$) anionic species.

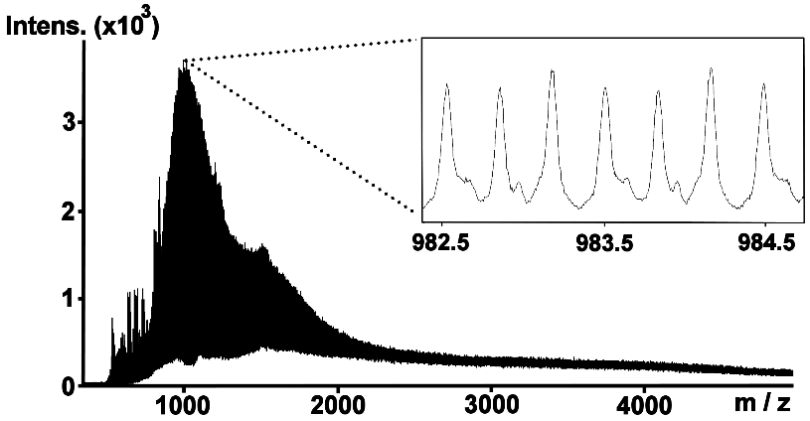


**Figure 4.** Negative ion mass spectrum of **1** in $H_2O$/MeCN. Inset: expanded distribution envelope of the discrete $\{Mo_{11}V_7O_{52}(TeO_3)\}$ POM. The peak separation of the distribution envelope reveals a triply charged ($z = -3$) anionic species.

**Electrochemistry.** Cyclic voltammetry was used to investigate the electrochemical behavior of each cluster and the electronic effect of the heteroanion on the reduction potential. The overall negative charge of the POM as well as the charge of the heteroanion is identical in each case while the study compares the redox behavior of the as the series is traversed with increasing atomic number. Voltammograms of **1** – **4** were recorded in 0.1 M acetate buffer solutions with $Na_2SO_4$ as supporting electrolyte.[40] Reduction potentials are referenced to the Ag/AgCl couple. The measurements were performed over the potential window ranging from 0 to +1.4 V at a scan rate in the range of 50 – 400 mV $s^{-1}$ towards the positive direction. The studies revealed that the quasi reversible redox wave which corresponds to a two-electron oxidation of both $V^{IV}$ centers as confirmed by controlled potential

coulometry. This behavior has been observed in similar vanadium-containing POMs,[41,42] indicating the $V^{IV}$ ions are electronically independent from each other. The reduction potential is modulated by the heteroanion, occurring at 0.60 V in **3**, and more positive values of 0.79 V and 0.86 V for the S- and P-based clusters, respectively (Figure 5). The reduction of the Te-containing POM is the most facile and shifts to even less positive potentials. In this case the redox wave is buried among other electrochemical processes, and overlaps with electrochemical events associated with the Mo/V metal centers located at the lower hemisphere of the POM leading to overlapped V-centered processes and a broad redox wave in the region of ca. 0.42 V (Figure S15). A clear trend to less positive potential is observed for this oxidation process traversing series **1** – **4** as a function of the electronegativity of the heteroatom as seen in related mixed-metal POMs (vide infra).[43]

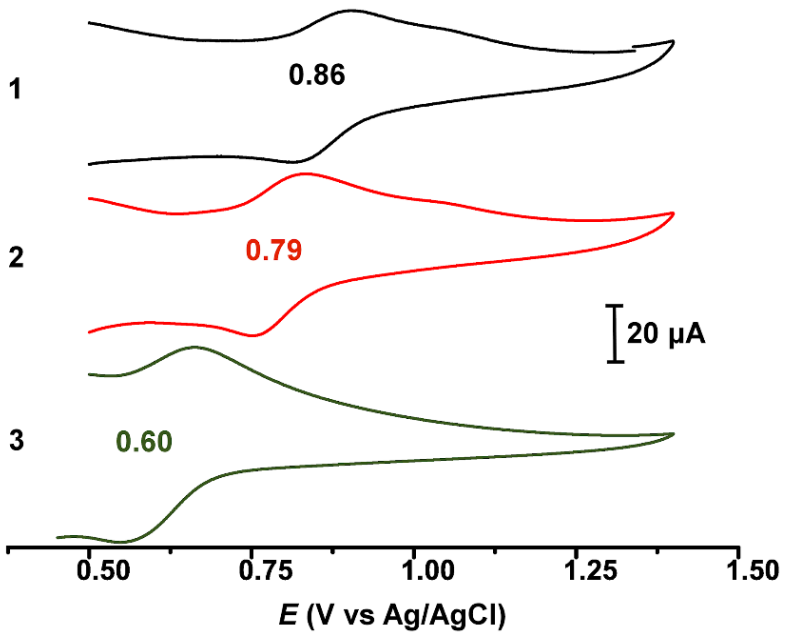


**Figure 5.** Comparison of the cyclic voltammograms of **1**, **2** and **3** recorded in 0.1 M acetate buffer (0.2 M $Na_2SO_4$ supporting electrolyte) at ambient temperature with a scan rate of 200 mV $s^{-1}$.

**Table 2.** Spin Hamiltonian Parameters from EPR Spectral Simulation

| | weight | $g_x$ | $g_y$ | $g_z$ | $\langle g \rangle$[a] | $\Delta g$[b] | Rhombicity[c] | $A_x$ | $A_y$ | $A_z$ | $\langle A \rangle$[d] | $k_\perp$ | $k_\parallel$ |
|---|---|---|---|---|---|---|---|---|---|---|---|---|---|
| **1** | 0.995 | 1.982 | 1.965 | 1.949 | 1.965 | 0.033 | 0.515 | 28 | 45 | 109 | 61 | 0.86 | 0.77 |
| | 0.005 | 1.983 | 1.969 | 1.945 | 1.966 | 0.038 | 0.368 | 57 | 59 | 130 | 82 | 0.84 | 0.80 |
| **2** | 0.860 | 1.986 | 1.964 | 1.947 | 1.966 | 0.039 | 0.564 | 42 | 53 | 128 | 74 | 0.77 | 0.79 |
| | 0.140 | 1.978 | 1.963 | 1.919 | 1.953 | 0.059 | 0.254 | 60 | 69 | 171 | 100 | 0.94 | 0.97 |
| **3** | | 1.982 | 1.962 | 1.951 | 1.965 | 0.031 | 0.645 | 28 | 45 | 108 | 60 | 0.86 | 0.76 |
| **4** | 0.975 | 1.976 | 1.966 | 1.948 | 1.963 | 0.028 | 0.357 | 32 | 45 | 122 | 66 | 0.98 | 0.78 |
| | 0.013 | 1.978 | 1.963 | 1.930 | 1.957 | 0.048 | 0.313 | 60 | 71 | 180 | 104 | 0.94 | 0.90 |
| | 0.012 | 1.981 | 1.964 | 1.922 | 1.956 | 0.049 | 0.347 | 60 | 69 | 168 | 99 | 0.88 | 0.95 |
| $[V^{IV}W_5O_{19}]^{4-}$ [e] | | 1.969 | 1.969 | 1.949 | 1.962 | 0.020 | 0 | 61 | 61 | 167 | 96 | ~1 | 0.77 |
| α-$[V^{IV}Mo_{11}O_{36}(PO_4)]^{5-}$ [f] | | 1.974 | 1.974 | 1.939 | 1.962 | 0.035 | 0 | 53 | 53 | 151 | 86 | ~1 | 0.84 |
| α-$[V^{IV}W_{11}O_{36}(PO_4)]^{5-}$ [f] | | 1.970 | 1.970 | 1.915 | 1.952 | 0.055 | 0 | 60 | 60 | 167 | 96 | ~1 | 0.99 |
| $\alpha_1$-$[V^{IV}W_{17}O_{54}(PO_4)_2]^{8-}$ [g] | | 1.970 | 1.970 | 1.917 | 1.952 | 0.053 | 0 | 53 | 53 | 166 | 91 | ~1 | 0.96 |
| $\alpha_2$-$[V^{IV}W_{17}O_{54}(PO_4)_2]^{8-}$ [g] | | 1.964 | 1.964 | 1.885 | 1.938 | 0.079 | 0 | 48 | 48 | 166 | 87 | ~1 | ~1 |
| $[V^{IV}O]^{2+}$ [h] | | 2.0153 | 1.9489 | 1.9155 | 1.960 | 0.100 | 0.665 | 63 | 92 | 193 | 116 | 0.86 | 0.98 |

[a] $\langle g \rangle = (g_x + g_y + g_z)/3$. [b] $g$-anisotropy, $\Delta g = g_x - g_z$. [c] Rhombicity = $(g_x - g_y)/(g_x - g_z)$. [d] $\langle A \rangle = (A_x + A_y + A_z)/3$. [e] Recorded at 77 K; data taken from ref. [44]. [f] Recorded at 77 K; data taken from ref. [43]. [g] Recorded at 77 K; data taken from ref. [45]. [h] Data for $[VO]^{2+}$ doped into single crystals of potassium oxalate monohydrate recorded at 293 K from ref. [46].

**EPR spectroscopy.** The presence of two paramagnetic $V^{IV}$ $d^1$ ions was confirmed by EPR spectroscopy on **1** – **4**; spectra recorded at X-band frequencies at 130 K on samples diluted in DMSO/$H_2O$ solutions are presented in Figure 6. Each cluster gives a signal consistent with $V^{IV}$ ions with the spectrum dominated by hyperfine coupling to the $^{51}V$ nucleus ($I$ = $^7/_2$, 99.75% natural abundance) generating the hallmark 8-line pattern. The appearance of the hyperfine structure can range from an axially-split 15-line pattern[44,47-53] to a broadened 8-line spectrum[13,45,54-57] to a completely isotropic profile[41,58,59] depending on the POM, the number of $V^{IV}$ ions, and their position in the cluster. However, it is mostly the sample – polycrystalline or frozen solution – and measurement conditions – temperature, frequency – that dictate the final outcome of EPR experiments.

The profile for **2** and **4** are similar, and more elaborate than for **1** and **3**. The spectrum of **3** is the most featureless: an isotropic 8-line splitting that spans ca. 100 mT consistent with uncoupled $V^{IV}$ $S$ = $^1/_2$ ions, i.e. the superposition of two monovanadium(IV) spectra. This is supported by the absence of a signal at half-field for forbidden transition that derives from the triplet ($S$ = 1) state of coupled $V^{IV}$ ions.[47,58] Interestingly the frozen solution and polycrystalline spectra, both recorded at 130 K, are identical (Figure S18). The hyperfine features are less pronounced in the room temperature spectrum though the overall spectral width is essentially the same. This indicates the appearance of the spectrum of **3** is dominated by intermolecular interactions, which are unperturbed when placed in solution. The most likely cause for the persistently large linewidth seen for **3** (cf. **1**, **2**, and **4**) is a dipolar broadening between neighboring units that are bound together through their $K^+$ counterions as seen in its solid state packing.[16] This is also an exchange coupling pathway, where the spins on neighboring clusters are coupling through the non-covalent bonds mediated by the terminal oxo groups and the $K^+$ counterions, and gives rise to exchange narrowing that reduces the linewidth in the center of the spectrum relative to the extremes.[60] This is less noticeable in **3** as the linewidths across the spectrum are essentially

uniform. The width is derived from the magnitude of the hyperfine interaction with the $^{51}V$ nuclei, and is noticeable weaker for **1** and **3** than **2** and **4**, however it is not possible to distinguish the intermolecular exchange interaction from the intrinsic one that can arise from neighboring $V^{IV}$ ions within the cluster. The superhyperfine coupling from the $V^{V}$ ions in the cluster will also contribute to the linewidth.[45,55]

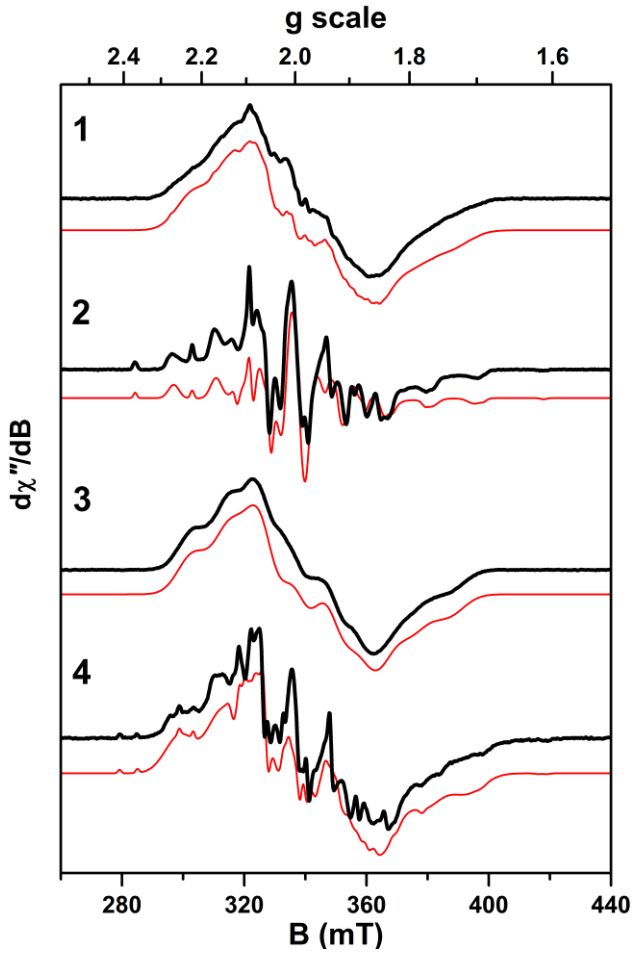


**Figure 6.** X-band EPR spectra of **1**–**4** in DMSO/$H_2O$ solution at 130 K. Experimental data are represented by the black line. Simulations are depicted by the red trace and parameters are summarized in Table 2.

The spectral width and profile for **1** is similar, though there is some weakly resolved hyperfine structure that is suggestive of overlapping signals rather than the result of defects in the DMSO/$H_2O$ glass. The polycrystalline samples recorded at 130 K and room temperature gave a single featureless line that is common encountered in spectra recorded on undiluted powders (Figure S16).[41,58,59] In the solid state, units of **1** forms oligomeric chains linked by their two $Na^+$ counterions (Figure 2). This interaction is seemingly less robust than in **3** when dissolved into the DMSO/$H_2O$ medium for the frozen solution spectrum (Figure S18), which displays a more complex lineshape profile indicative of a second signal with narrower lines sitting beneath the dominant isotropic one.

The EPR spectrum of **2** is the most informative (Figure 6). By visual inspection it can be seen to be composed of two subspectra, with the dominant species having a similar isotropic profile based on the resonance position and number of lines to that of **3**. However, unlike in **1** and **3**, the inner lines at the resonance position are significantly more resolved. The second component has sharper lines and spans ca. 160 mT, where the outer most hyperfine lines are clearly resolved. This subspectrum is characteristic of a monovanadium(IV) with its axial symmetry where the parallel hyperfine component, $A_{\|}$, is larger than perpendicular component, $A_{\perp}$ (vide infra).[44,46,48,53] There are at least three components that comprise the EPR spectrum of **4**, with the broad lines on the isotropic component and a miniscule contribution from two axial signals identical to that seen in **2**.

The EPR spectra have been simulated using the spin-Hamiltonian defined as in Eq. 1:

$$\hat{H} = \mu_B \mathbf{B}\cdot\mathbf{g}\cdot\mathbf{S} + \mathbf{S}\cdot\mathbf{A}\cdot\mathbf{I} \qquad (1)$$

where **g** and **A** are the 3×3 electron Zeeman and magnetic hyperfine interaction matrices, respectively. Oxovanadium(IV) EPR spectra are characterized as highly axial symmetry with $g_{\|}$ (= $g_z$) < $g_{\perp}$ (= $g_x$, $g_y$) < $g_e$ (= 2.0023). The hyperfine splitting is also axial with $A_{\|} > A_{\perp}$,[61] and these are the parameters that describe the $^2B_2$ ground state ($d_{xy}$ orbital) of the $[VO]^{2+}$ unit possessing $C_{4v}$ symmetry where the *z*-axis

is parallel to the V≡O bond.[62] However, the presence of two of these centers in different locations across the nine available sites of the lower hemisphere of the cluster where the neighbors will vary ($V^V$ and $Mo^{VI}$) means these paramagnetic centers will trend closer to orthorhombic symmetry, i.e. $g_x \neq g_y$ and $A_x \neq A_y$. Despite this, we maintain the **g** and **A** axes are coincident due to the lack experimental resolution to allow inclusion of noncoincidence angles. With the exception of **3**, a satisfactory simulation was only achieved by carefully weighting the contributing subspectra to the total signal (Figure 6). The spin-Hamiltonian parameters for each subspectrum and relative contribution to the simulation are compiled in Table 2.

The spectrum of **3** was simulated as a single $S = {}^1/_2$ species with a large linewidth that masks the anisotropy and rhombicity of the principal *g*-values. As such it shows the greatest departure from axiality when compared with a single $V^{IV}$ center in related POMs such as $[PV^{IV}W_{11}O_{40}]^{5-}$,[53] however orthorhombic spectra have been diagnosed in related Dawson structures,[50] and more notably in $[VO]^{2+}$-doped single crystals.[46] The most stark difference are the small hyperfine coupling constants, which are uniformly smaller than for the single oxovanadium(IV) species, which is to say the *A*-anisotropy remains the same it is just there is less spin density on the $V^{IV}$ ion. This is symptomatic across the series as the dominant component to the spectrum have similar principal *g*- and *A*-values (Table 2). Similar in profile, **1** was simulated using identical parameters to **3**. In addition, a miniscule (0.5%) second species was overlaid to account for the spectral profile, which has similar *g*-values but larger hyperfine coupling that account for the breadth of the experimental spectrum.

The spectrum of **2** was simulated by combining two subspectra. The main constituent has the similar spin-Hamiltonian parameters as **3** but with a substantially smaller linewidth, larger *g*-anisotropy and hyperfine coupling suggests this cluster is well separated from its neighbors and therein the input from intermolecular interactions. The second species accounts for 14% of the overall signal, with spin-

Hamiltonian parameters much like the classical vanadyl spectrum,[45,47,48,50-53,63] and less rhombic that the major component. This signal does not stem from decomposition releasing vanadyl-containing fragments as these would appear in the mass spectrum (vide supra). Furthermore, **2** has a room temperature magnetic moment of 2.36 $\mu_B$ in DMSO-$d_6$ determined by NMR. This corresponds to two uncoupled $S = {}^1/_2$ centers with $g = 1.93$, which is very close average $g$-value for **2** (Table 2). On the whole there is an intensity mismatch with the experimental possessing more signal around ca. 320 mT than in the simulation, which potentially suggests a third subspectrum, one that is featureless and isotropic. The EPR spectrum of polycrystalline **2** has been reported,[13] yielding $g$ = (1.981, 1.965, 1.946), and $A$ = (45, 45, 137) × $10^{-4}$ $cm^{-1}$ from a multifrequency (X-, K-, and W-band) investigation at 10 K. These are essentially the same as the major component recorded here in a DMSO/$H_2O$ frozen glass at 130 K, although the higher temperature data gives rise to broader lines. Simulation of **4** required three subspectra; the main component has spin-Hamiltonian parameters most similarly to **3**. There are two noticeable differences, namely **4** has the lower $g_x$ than **3**, which we ascribe to the effect of the colossal Te spin-orbit coupling constant of 3950 $cm^{-1}$ (cf. 1700 $cm^{-1}$ for Se).[64] Secondly, the $A_z$ value is larger for **4** than **3**, and further suggests the small value in the latter stems from intermolecular interactions orchestrated by its $K^+$ counterions which are absent in **4**. There are two minor signals with noticeably sharp lines that account for 2.5% of the overall spectrum. They are equally weighted, where the subspectrum with the smaller width has parameters identical to the minor component of **2**, and the other has a slightly larger $A_z$ value.

EPR studies of paramagnetic polyoxometalates have catalogued a number of contributions to the profile of the spectrum. The salient contribution in vanadyl-substituted POMs is dictated by the neighboring metal ions and the connectivity between adjacent polyhedra which varies according to the architecture, such as edge-shared in the Lindqvist ion, alternating edge-shared and corner-shared in the

Keggin and Dawson ions.[65] This is exemplified by a comparison of POMs with the inclusion of single $V^{IV}$ ion included in Table 2 as their parameters act as a useful guide. The *g*-anisotropy of the $V^{IV}$ in the Lindqvist ion is considerably less than the Keggin and Dawson ions, specifically a larger $g_{\|}$ ($g_z$) value, and is diagnostic of adjacent edge-shared $MO_6$ polyhedra. The intermetal distance is shorter in edge-shared octahedra, and allows the neighboring metal ions greater interaction with the vanadyl center either via the bridging oxo ligands or direct overlap of d orbitals. This observation is relevant here to diagnose the isomers that give rise to the two distinct signals in **2** and **4** (Figure 6). From the single $V^{IV}$ POMs, the variation in $g_z$ stems from spin-orbit coupling from the adjacent Mo or W ions. For $d^1$ metal ions in an axially distorted octahedron ($C_{4v}$), the *g*-values can be represented as:[66]

$$g_{\|} = g_e - 8\lambda_0 k_{\|}^2/\Delta E(B_2 \rightarrow B_1) \quad (2)$$

$$g_{\perp} = g_e - 2\lambda_0 k_{\perp}^2/\Delta E(B_2 \rightarrow E) \quad (3)$$

where $\lambda_0$ is the spin-orbit coupling constant for a free ion, $\Delta E(B_2 \rightarrow B_1)$ and $\Delta E(B_2 \rightarrow E)$ are the energies of the $d_{xy} \rightarrow d_{x^2-y^2}$ and $d_{xy} \rightarrow d_{xz,yz}$ ligand field transitions, respectively, of the tetragonally distorted oxovanadium(IV) center, and $k_{\|}$ and $k_{\perp}$ are parameters that represent the degree of covalency in V–O bonds along the *z*-axis and in the *xy* plane, respectively. For pure ionic bonds, these parameters take a value of unity. The spin-orbit coupling constant for $V^{IV}$ is 170 $cm^{-1}$,[67] and the ligand field transition energies are experimentally measured at 12,407 $cm^{-1}$ and 15,200 $cm^{-1}$ from the representative electronic spectrum, that of **2** (Figure S20). However, any increase in bond covalency provided by the larger, more diffuse 4d and 5d orbitals of Mo and W ions would also reduce the $^{51}V$ hyperfine interaction as spin density is filtered away from the $V^{IV}$ ion. However, the *A*-values are invariant, therefore the higher $g_z$ value for molybdovanadates compared with tungstovanadates is a consequence of low energy charge-transfer excited states that mix with the ground state via spin-orbit coupling.[53] Although tungsten has a larger spin-orbit coupling constant, the heteronuclear intervalence

charge transfer (IVCT) transition,[68] $V^{IV} \rightarrow W^{VI}$ is typically above 20,000 $cm^{-1}$.[45,53,55] The analogous $V^{IV} \rightarrow Mo^{VI}$ IVCT transition is lower in energy, 16,000 – 18,000 $cm^{-1}$,[43,50,54] and therefore this effect is conceivably more potent leading to Mo contributions to the ground state that boosts $g_z$ more so than $g_{x,y}$ (Eq. 2 and 3). As the lesser component of the EPR spectrum of **2** has parameters similar to single $V^{IV}$ substituted POMs, and that this signal derives from a $V^{IV}$ center with only $Mo^{VI}$ neighbors. This would be the case of one $V^{IV}$ in the $M_6$ belt, with two edge-shared $Mo^{VI}$ and two corner-shared $Mo^{VI}$ neighbors, where one of these is the in the upper hemisphere of the cluster (Figure 7). There is also a link to the tetrahedral $VO_4$ centers of the upper hemisphere, however this coupling is negligible.[50] Assuming a random distribution of isomers, that is all combinations of the 5 $Mo^{VI}$, 2 $V^{V}$, and 2 $V^{IV}$ distributed across the nine sites of the lower hemisphere, as commonly encountered with molybdovanadates,[50] the probability of this particular configuration is 12%. This matches very nicely to the 14% calculated from the simulation. This isomer is identified in **4**, though constitutes a paltry 1.2% on the sample and indicates that the spread of is not random but related to the heteroanion, either due to size or electronic properties, though most likely both. Certainly the isolated $V^{IV}$ isomer with this unique signal is not seen for **1** and **3**, either in the solid state at cryogenic and ambient temperature (Figures S13 and S15). The second highly anisotropic signal observed in the spectrum of **4** is most likely the result of the result of decomposition: in DMSO solution and the facile reduction potential provided by the $TeO_3^{2-}$ heteroanion in **4** leads to trace $[VO]^{2+}$ (1.3%), and absent from the polycrystalline sample (Figure S19).

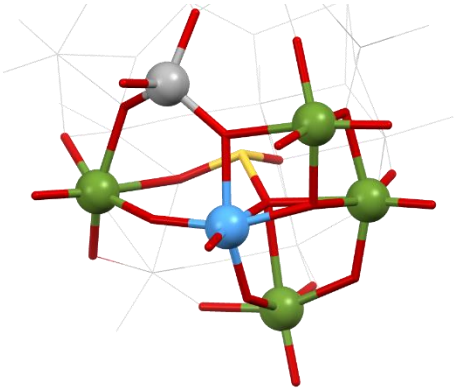

**Figure 7.** Depiction of the isomer that gives the minor signal (14%) in the EPR spectrum of **2**: the $V^{IV}$ $S = {}^{1}/_{2}$ ion (cerulean) situated in the $M_6$ belt connected to four $Mo^{VI}$ ions (olive) and a $V^{V}$ ion (cement) in the tetrahedral site of the upper hemisphere.

Therefore the remaining isomers essentially give the same spectrum. The bulk of the signal has spin-Hamiltonian parameters dissimilar to the classic vanadyl and are commonly encountered in mixed-valence systems where more than one vanadium ion is present in both the +IV and +V oxidation states.[43-45,48,49,52-55,57,63] The driving force behind the reduced *g*-anisotropy and broad lines comes from electron hopping from the donor $V^{IV}$ centers to adjacent acceptor $V^{V}$ ions. The $V^{IV} \rightarrow V^{V}$ IVCT transition is found in the near infrared region of the spectrum, below 9000 $cm^{-1}$.[43,45,55] This makes the electron transfer extremely facile, and dependent on the V–O–V angle. For Lindqvist ions, where all octahedral are edge-shared, the process is limited as the average 125° angle is not optimal for $d_{\pi}$–$p_{\pi}$–$d_{\pi}$ overlap through which the unpaired electron in the vanadyl $d_{xy}$ orbital can transfer to an adjacent $V^{V}$ center.[45,54,57] At room temperature a 15-line spectrum is observed from coupling of the electron spin to two equivalent $^{51}V$ nuclei, both as a polycrystalline material or in solution.[45,49,52,54,55,57,69]

At lower temperatures, and depending on the connectivity of the POM, the electron becomes localized. For example, the electron in $[PV_2W_{16}O_{62}]^{9-}$ is localized at 211 K as it the vanadium ions occupy edge-shared sites on the $M_3$ cap.[45] In contrast, corner-shared, mixed-valent $V^{V}/V^{IV}$ moieties connected

through more obtuse V–O–V angles up to 150°,[65] the unpaired electron is still delocalized to the adjacent $V^{V}$ ion down to 10 K.[54,70] Interestingly, protonation of one bridging oxo ligand destroys the efficiency of the $d_{\pi}$–$p_{\pi}$–$d_{\pi}$ overlap in a similar manner to positioning a group 6 ion between $V^{IV}$ and $V^{V}$ ions.[45,51,52,54,55] This is the situation with these clusters, where the remaining isomers will have at least one $V^{V}$ ion adjacent the paramagnetic $V^{IV}$. Therefore, the profile of the signal will be similar, as the electron hopping between corner-sharing octahedra, which link the three edge-shared octahedra in the $M_6$ belt and each metal site of the $M_3$ cap. This leads to delocalization of the electron even down to 10 K, as multifrequency measurements on polycrystalline **2** confirm.[13] At this temperature the electron is mostly localized though with some contribution from neighboring $V^{V}$ ions manifest as line broadening. By this mechanism, the electron density at the $V^{IV}$ center is lowered, commensurate with the attenuated *A*-values compared to the minor component of the spectrum of **2** (Table 2). When the values $g_z$ = 1.947 and $g_x$ = 1.986 (as a reasonable value for $g_{\perp}$) are added to equations 2 and 3, respectively, $k_{\parallel}$ and $k_{\perp}$ are computed as 0.79 and 0.77. The deviation from unity is a measure of the degree covalency in the bonds about the $V^{IV}$ ions in the cluster. The terminal oxo ligand is inherently covalent on account of its short distance (ca. 1.6–1.7 Å) and multiple bond character.[62] For each cluster, the major component of the EPR spectrum gives the same $k_{\parallel}$ value, 0.76–0.79 (Table 2). The in-plane covalency is greater for the major signal, and this stems from the delocalization of the unpaired electron through the bridging oxo ligands to neighboring $V^{V}$ ions. The orthorhombicity observed with these spectra result from different metal ions, $V^{V}$ and $Mo^{IV}$ either side of the vanadyl, which breaks the symmetry of the in-plane V–O bonds. For **1** – **4**, a similar trend in the in-plane bond covalency is observed, as defined by $k_{\perp}$ (Table 2). The minor species in the spectra of **2** and **4** that have a more classic vanadyl profile – a $V^{IV}$ center without adjacent $V^{V}$ ions to accept electrons. This isomer is saturated at 10 K and therefore absent from

spectra recorded on polycrystalline **2**,[13] whereas it is visible in the spectrum recorded at 130 K with some features in the low field extremity that are indicative of electron hopping.[49,52,54]

**DFT calculations.** The electronic structure and redox properties of these clusters was investigated using density functional theoretical (DFT) calculations of the series. Each cluster was geometry optimized at the BP86 level of theory, and given their high charge, a water solvation shell was constructed defined by van der Waal radii of the vanadium, molybdenum and oxygen atoms.[17,71] The rigidity of these species is evidenced by the meager differences between the optimized the crystallographic structures (Table 3). Overall the optimized clusters are ~0.05 Å taller and 0.2 Å wider, with no discernable change to the bond and angles about the heteroanion. With the heteroanions unchanged, the distance from its oxygen atoms to the surface metal ions increases compared to the solid state structure.

The distribution of the four vanadium ions over the nine available sites of the lower hemisphere was chosen arbitrarily. For these calculated models, two went into the $M_3$ cap and the other two the $M_6$ belt; 44% of all possible isomers possess this arrangement. Upon this structure, the calculation upon a spin multiplicity of 3 would add two unpaired electrons. These were found to be positioned in the lower hemisphere in keeping as demonstrated by BVS calculations (vide supra). The Mulliken spin population analysis reveals these unpaired electrons are delocalized over all nine metal ions, and does not distinguish individual $V^{IV}$ and $V^{V}$ centers (Figure 8).

**Table 3.** Comparison of Salient Experimental and Optimized Structural Metrics[a]

| E | $[Mo_{11}V_7O_{52}(EO_3)]^{7-}$ | height[b] | width[c] | O–E–O[d] | E···$O_3$[e] | $M_6$–O(–E)[f] | $M_3$–O(–E)[g] |
|---|---|---|---|---|---|---|---|
| **PH** | *experimental* | 8.884 | 7.175 | 110.7 | 0.479 | 2.412 | 2.412 |
| | *calculated* | 8.926 | 7.334 | 110.8 | 0.481 | 2.443 | 2.534 |
| **S** | *experimental* | 8.901 | 7.135 | 103.5 | 0.652 | 2.453 | 2.397 |
| | *calculated* | 8.937 | 7.325 | 103.2 | 0.667 | 2.496 | 2.508 |
| **Se** | *experimental* | 8.838 | 7.150 | 99.3 | 0.809 | 2.352 | 2.320 |
| | *calculated* | 8.919 | 7.331 | 99.6 | 0.817 | 2.414 | 2.473 |
| **Te** | *experimental* | 8.852 | 7.170 | 95.2 | 0.977 | 2.309 | 2.326 |
| | *calculated* | 8.901 | 7.337 | 94.9 | 1.000 | 2.344 | 2.439 |

[a] Distances in Å; angles in degrees. [b] Defined as the distance from the apical $\mu_3$-O of the upper hemisphere with the centroid of the $M_3$ base of the lower hemisphere. [c] Defined as the average distance between the Mo ions of the six-membered ($Mo_3V_3$) belt of the upper hemisphere. [d] Average bond angle in the $EO_3^{2-}$ unit. [e] Distance of E atom above $O_3$ plane in the $EO_3^{2-}$ unit. [f] Average M–O bond distance between $M_6$ belt of lower hemisphere and oxygen atoms of the $EO_3^{2-}$ unit. [g] Average M–O bond distance between $M_3$ base of the lower hemisphere and oxygen atoms of the $EO_3^{2-}$ unit.

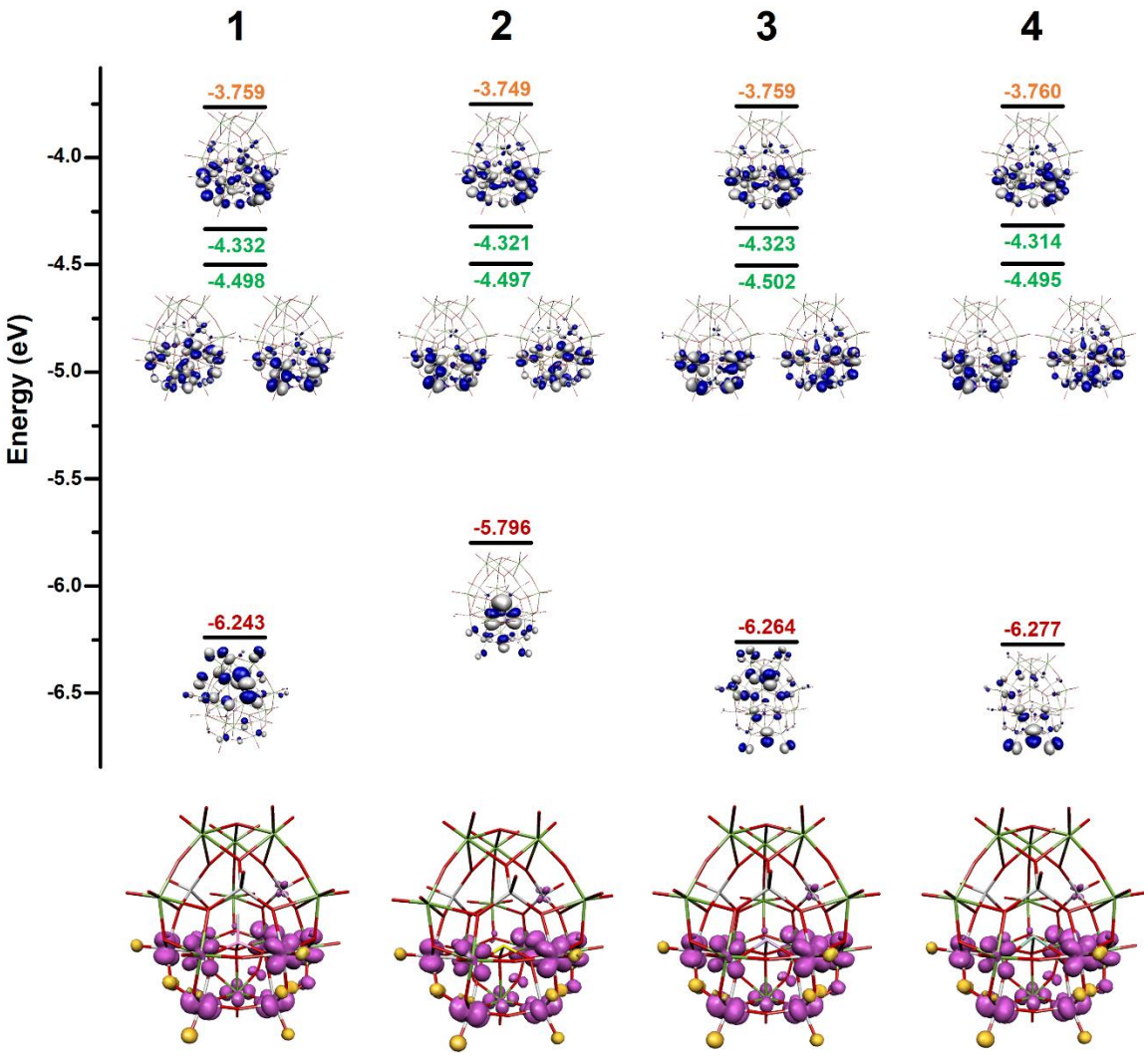


**Figure 8.** Top: comparison of the computed energies of the frontier MOs for **1**–**4** from ZORA-BP86 DFT calculations. The energies of the two SOMOs are labelled in green, the energy of the LUMO in orange, and the HOMO-2 labelled in red. Bottom: Mulliken spin density population (α-spin: lilac; β-spin: saffron).

The vanadium ions carry slightly more spin density than their $Mo^{VI}$ counterparts. This is marked by a quotient of β-spin on the six coordinated oxo ligands to each vanadium ion, which arises from bond polarization underscoring the ionicity of the V–O bonds (vide supra). The bonds about the larger $Mo^{VI}$ ions are more covalent and thus no spin density is deposited on their first coordination sphere oxo

ligands (unless linked to a vanadium ion). The two singly-occupied molecular orbitals (SOMO) from which the spin density distribution is derived are near degenerate, with a consistent energy separation of 0.17 eV across the series (Figure 8). These orbitals, which are composed of combinations of metal $d_{xy}$ orbitals, comprise an E set in three-fold symmetry, but the lowering of symmetry because of the mix of metal ions in the lower hemisphere gives the calculated energetic splitting of these SOMOs; the third orbital related to these SOMOs is the $A_1$ symmetric LUMO. The energy separation will shift for the different isomers, and may even switch their energetic ordering. The HOMO-2 orbital, the highest doubly occupied MO, shows the greatest variation across the series, which would make it dependent on the heteroatom. For **1**, the MO is mainly confined to the apex of the cluster. The involvement of oxo ligand p orbitals from the lower hemisphere to this MO increases in **3** where a selenite sits at the core. In the heaviest cluster, this MO is predominantly localized to the basal $M_3$ cap. For **2**, the HOMO-2 is unique, and is the lone pair of the sulfur atom in the sulfite template. This demonstrates than as the principal quantum number is increased from 3p in **1** and **2**, to 4p in **3**, and 5p in **4**, the energy of the lower hemisphere is destabilized above the upper hemisphere. This will contribute to the observed reduction potentials, as the decrease in E–O covalency makes the oxidation processes more facile (vide supra).

The influence of the heteroatom on the electronic structure of these Dawson-like clusters is not immediately apparent from the MO diagram because of the large number of orbitals that contribute to the physical properties of these clusters. Moreover, the contributions of the heteroatom to the frontier MOs is almost negligible. However, the charge and size of the heteroatom effects the covalency of the E–O bonds and therein the basicity of these oxo ligands that are coordinated to the nine metal ions of the lower hemisphere. Larger $SeO_3^{2-}$ and $TeO_3^{2-}$ heteroanions are able to position their oxygen atoms closer to the metallic shell (Table 3) which effects the covalency of the terminal oxo ligands trans to

this bond. Herein is the impact of the heteroanion, similar to an inductive effect primarily through the σ-bond pathway from the heteroatom to the transition metal ions. The electronegativity of the heteroatom in the $EO_3^{2-}$ ion can be gauged by its Hirshfeld charge. These have been calculated for this series with P +0.45, S +0.42, Se +0.60, Te +0.78. The latter has the most positive Hirshfeld charge and is thus the least electronegative heteroatom in this series; the overall trend perfectly matches the shift toward more positive reduction potentials as the series is traversed (Figure 9). The effect of decreasing electronegativity of the heteroatom limits its capacity to syphon electron density away from the metal oxide shell and making the loss of charge (oxidation) more facile.

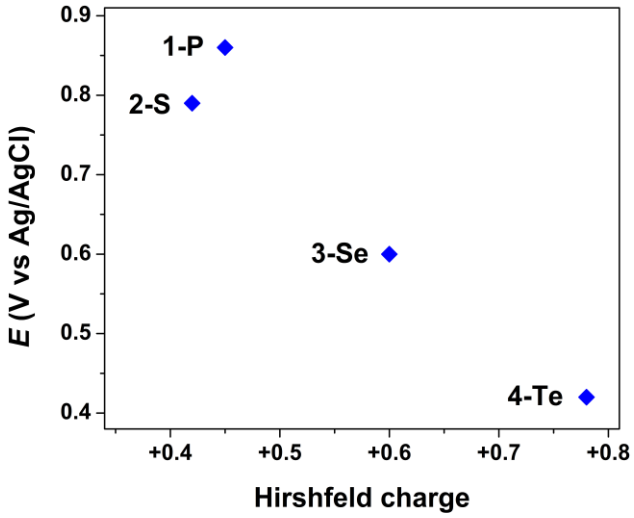


**Figure 9.** Correlation of calculated Hirshfeld charge versus reduction potential for **1** – **4**.

## Conclusions

In the present work we reported the synthesis and characterization of two new heterometallic mixed-valent molybdovanadate POMs, namely: $(Me_2NH_2)_5Na_2[Mo_{11}V^{V}_5V^{IV}_2O_{52}(HPO_3)]\cdot MeOH\cdot 5H_2O$ (**1**) and $(Me_2NH_2)_6Na[Mo_{11}V^{V}_5V^{IV}_2O_{52}(TeO_3)]\cdot 15H_2O$ (**4**), together with $(NH_4)_7[Mo_{11}V^{V}_5V^{IV}_2O_{52}(SO_3)]\cdot 12H_2O$ (**2**) and $K_7[Mo_{11}V^{V}_5V^{IV}_2O_{52}(SeO_3)]\cdot 31H_2O$ (**3**) make a four

member series. Within this family we examine effect of the changing identity of the heteroatom on the molecular and electronic structure of cluster. Experimental data corroborated by theoretical studies revealed that the two unpaired electrons are confined to the lower hemisphere, where two out of nine metal sites have a paramagnetic $V^{IV}$ ion. They are seemingly distributed stochastically giving rise to a continuum of isomers. The existence of these isomers, as well as the temperature, solvation, and counterion dependence of the EPR signal hamper an unambiguous assignment of the spectra. Despite these challenges, we have identified the unique EPR signal stems from the isomer with a $V^{IV}$ ion with only $Mo^{VI}$ centers located in the adjacent octahedra, which is readily distinguished from the signal for the remaining isomers that have at least one neighbouring $V^{V}$ ion. The relative intensity of this signal in the spectrum of **2** suggests there is a statistical distribution of all possible isomers (arranging four V ions over nine sites). Although the same signal is observed for **4**, though only 1.2% abundance, it is absent in the spectra of **1** and **3**. This is because of associated factors that impact the EPR spectra rather than a particular preference of the heteroatom on the isomer distribution. It is most likely a statistical distribution, which is prevalent for molybdovanadate POMs,[50] and the utility of the EPR spectra are in this case, dependent on the counterions. We have revealed that the charge on the heteroatom follows the trend S < P < Se < Te, which is neatly correlated to the reduction potential, specifically the two-electron oxidation of the cluster, where the smaller heteroatoms confer a positive shift of the reduction potential ascribed as an inductive effect that lowers the charge on the metal oxide shell. The main group template in these constructs act as electronic and assembly modulator offering the opportunity to develop bottom-up design approaches for the assembly of nanostructured clusters which can be used as modular functional units in molecular electronics applications.

**Acknowledgments**

We gratefully acknowledge financial support from the University of Glasgow, the EPSRC (grants EP/L023652/1, EP/K023004/1, EP/H024107/1, EP/I033459/1 and EP/J015156/1) and the ERC (project 670467 SMART-POM) for supporting this work.

**Electronic Supplementary Information (ESI) available:** Additional experimental characterization, IR, CV, EPR and electronic spectra, TGA profiles, crystallographic bond distances and angles, optimized coordinates, Mulliken spin density plots. See DOI: 10.1039/x0xx00000x

**References**

[1] a) *Metal Oxide Chemistry and Synthesis: From Solution to Solid State*, John Wiley & Sons Ltd, Chicester, England, **2000**; b) *Polyoxometalates: From Topology via Self-Assembly to Applications*, Kluwer Academic, Dordrecht, **2001**; c) *Polyoxometalate Chemistry for Nanocomposite Design*, Kluwer Academic, New York, **2002**; d) D.-L. Long, R. Tsunashima, L. Cronin, *Angew. Chem. Int. Ed.* **2010**, *49*, 1736; e) H. N. Miras, J. Yan, D.-L. Long, L. Cronin, *Chem. Soc. Rev.* **2012**, *41*, 7403; f) M. T. Pope, A. Müller, *Angew. Chem. Int. Ed.* **1991**, *30*, 34.

[2] J.-J. Chen, M. D. Symes, S.-C. Fan, M.-S. Zheng, H. N. Miras, L. Cronin, *Adv. Mater.* **2015**, *27*, 4649.

[3] a) J.-D. Compain, P. Mialane, A. Dolbecq, I. M. Mbomekallé, J. Marrot, F. Sécheresse, E. Rivière, G. Rogez, W. Wernsdorfer, *Angew. Chem. Int. Ed.* **2009**, *48*, 3077; b) M. Ibrahim, Y. Lan, B. S. Bassil, Y. Xiang, A. Suchopar, A. K. Powell, U. Kortz, *Angew. Chem. Int. Ed.* **2011**, *50*, 4708; c) M. Ibrahim, Y. Xiang, B. S. Bassil, Y. Lan, A. K. Powell, P. de Oliveira, B. Keita, U. Kortz, *Inorg. Chem.* **2014**, *52*, 8399; d) C. Richie, A. Ferguson, H. Nojiri, H. N. Miras, Y.-F.

Song, D.-L. Long, E. Burkholder, M. Murrie, P. Kögerler, E. K. Brechin, L. Cronin, *Angew. Chem. Int. Ed.* **2008**, *47*, 5609.

[4] a) L. D'Souza, M. Noeske, R. M. Richards, U. Kortz, *Appl. Catal., A.* **2013**, *453*, 262; b) I. M. Mbomekallé, B. Keita, L. Nadjo, P. Berthet, K. I. Hardcastle, C. L. Hill, T. M. Anderson, *Inorg. Chem.* **2003**, *42*, 1163; c) N. Mizuno, K. Yamaguchi, K. Kamata, *Coord. Chem. Rev.* **2005**, *249*, 1944; d) R. Neumann, A. M. Khenkin, I. Vigdergauz, *Chem. Eur. J.* **2000**, *6*, 875.

[5] a) K. Nomiya, H. Torii, T. Hasegawa, Y. Nemoto, Y. Nomura, K. Hashino, M. Uchida, Y. Kato, K. Shimizu, M. Oda, *J. Inorg. Biochem.* **2001**, *86*, 657; b) J. T. Rhule, C. L. Hill, D. A. Judd, R. F. Schinazi, *Chem. Rev.* **1998**, *98*, 327.

[6] a) G. Bernardini, A. G. Wedd, C. Zhao, A. M. Bond, *Dalton Trans.* **2012**, *41*, 9944; b) C. R. Graham, R. G. Finke, *Inorg. Chem.* **2008**, *47*, 3679; c) M. Haouas, I.-M. Mbomekallé, N. Vila, P. de Oliveira, F. Taulelle, *Inorg. Chem.* **2014**, *53*, 5568; d) I. M. Mbomekallé, Y. W. Lu, B. Keita, L. Nadjo, *Inorg. Chem. Commun.* **2004**, *7*, 893; e) T. Ueda, M. Ohnishi, D. Kawamoto, S.-X. Guo, J. F. Boas, A. M. Bond, *Dalton Trans.* **2015**, *44*, 11660; f) Y. Yang, S. Liu, C. Li, S. Li, G. Ren, F. Wei, Q. Tang, *Inorg. Chem. Commun.* **2012**, *12*, 54.

[7] a) S. Himeno, A. Saito, T. Hori, *Bull. Chem. Soc. Jpn* **1990**, *63*, 1602; b) U. Kortz, M. T. Pope, *Inorg. Chem.* **1994**, *33*, 5643.

[8] D.-L. Long, Y.-F. Song, E. F. Wilson, P. Kögerler, S.-X. Guo, A. M. Bond, J. S. J. Hargreaves, L. Cronin, *Angew. Chem. Int. Ed.* **2008**, *47*, 4384.

[9] J. Yan, D.-L. Long, E. F. Wilson, L. Cronin, *Angew. Chem. Int. Ed.* **2009**, *48*, 4376.

[10] M. J. Manos, J. D. Woollins, A. M. Z. Slawin, T. A. Kabanos, *Angew. Chem. Int. Ed.* **2002**, *41*, 2801.

[11] D.-L. Long, P. Kögerler, L. Cronin, *Angew. Chem. Int. Ed.* **2004**, *43*, 1817.

[12] a) G. I. Chilas, H. N. Miras, M. J. Manos, J. D. Woollins, A. M. Z. Slawin, M. Stylianou, A. D. Keramidas, T. A. Kabanos, *Pure Appl. Chem.* **2005**, *77*, 1529; b) M. J. Manos, H. N. Miras, V. Tangoulis, J. D. Woollins, A. M. Z. Slawin, T. A. Kabanos, *Angew. Chem. Int. Ed.* **2003**, *42*, 425; c) H. N. Miras, R. G. Raptis, P. Baran, N. Lalioti, A. Harrison, T. A. Kabanos, *C. R. Chimie* **2005**, *8*, 957; d) H. N. Miras, R. G. Raptis, N. Lalioti, M. P. Sigalas, P. Baran, T. A. Kabanos, *Chem. Eur. J.* **2005**, *11*, 2295.

[13] H. N. Miras, D. J. Stone, E. J. L. McInnes, R. G. Raptis, P. Baran, G. I. Chilas, M. P. Sigalas, T. A. Kabanos, L. Cronin, *Chem. Commun.* **2008**, 4703.

[14] H. N. Miras, M. N. Corella Ochoa, D.-L. Long, L. Cronin, *Chem. Commun.* **2010**, *46*, 8148.

[15] M. N. Corella-Ochoa, H. N. Miras, A. Kidd, D.-L. Long, L. Cronin, *Chem. Commun.* **2011**, *47*, 8799.

[16] M. N. Corella Ochoa, H. N. Miras, D.-L. Long, L. Cronin, *Chem. Eur. J.* **2012**, *18*, 13743.

[17] Q. Zheng, L. Vilà-Nadal, C. Busche, J. S. Mathieson, D.-L. Long, L. Cronin, *Angew. Chem. Int. Ed.* **2015**, *54*, 7895.

[18] D.-L. Long, H. Abbas, P. Kögerler, L. Cronin, *Angew. Chem. Int. Ed.* **2005**, *44*, 3415.

[19] H. N. Miras, M. Sorus, J. Hawkett, D. O. Sells, E. J. L. McInnes, L. Cronin, *J. Am. Chem. Soc.* **2012**, *134*, 6980.

[20] C. Busche, L. vilà-Nadal, J. Yan, H. N. Miras, D.-L. Long, V. P. Georgiev, A. Asenov, R. H. Pedersen, N. Gadegaard, M. M. Mirza, D. J. Paul, J. M. Poblet, L. Cronin, *Nature* **2014**, *515*, 545.

[21] a) Q. Han, X. Sun, J. Li, P. Ma, J. Niu, *Inorg. Chem.* **2014**, *53*, 2006; b) Y. Jeannin, J. Martin-Frere, *Inorg. Chem.* **1979**, *18*, 3010; c) Y. Ozawa, Y. Sasaki, *Chem. Lett.* **1987**, *16*, 923; d) J.

Wang, P. Ma, J. Zhao, J. Niu, *Inorg. Chem. Commun.* **2007**, *10*, 523; e) J. Yan, D.-L. Long, L. Cronin, *Angew. Chem. Int. Ed.* **2010**, *49*, 4117.

[22] G. M. Sheldrick, *Acta Crystallogr. Sect. A* **1990**, *46*, 467.

[23] G. M. Sheldrick, *Acta Crystallogr. Sect. A* **2008**, *64*, 112.

[24] L. J. Farrugia, *J. Appl. Cryst.* **1999**, *32*, 837.

[25] R. C. Clark, J. S. Reid, *Acta Crystallogr. Sect. A* **1995**, *51*, 887.

[26] S. Stoll, A. Schweiger, *J. Magn. Reson.* **2006**, *178*, 42.

[27] F. Neese, *WIREs Comput. Molec. Sci.* **2012**, *2*, 73.

[28] a) A. D. Becke, *J. Chem. Phys.* **1988**, *84*, 4524; b) J. P. Perdew, *Phys. Rev. B* **1986**, *33*, 8822.

[29] D. A. Pantazis, X.-Y. Chen, C. R. Landis, F. Neese, *J. Chem. Theory Comput.* **2008**, *4*, 908.

[30] a) E. van Lenthe, J. G. Snijders, E. J. Baerends, *J. Chem. Phys.* **1996**, *105*, 6505; b) E. van Lenthe, A. van der Avoird, P. E. S. Wormer, *J. Chem. Phys.* **1998**, *108*, 4783; c) J. H. van Lenthe, S. Faas, J. G. Snijders, *Chem. Phys. Lett.* **2000**, *328*, 107.

[31] a) R. Ahlrichs, K. May, *Phys. Chem. Chem. Phys.* **2000**, *2*, 943; b) F. Weigend, R. Ahlrichs, *Phys. Chem. Chem. Phys.* **2005**, *7*, 3297.

[32] a) A. Klamt, *J. Phys. Chem.* **1995**, *99*, 2224; b) A. Klamt, V. Jonas, *J. Chem. Phys.* **1996**, *105*, 9972; c) A. Klamt, G. Schüürmann, *J. Chem. Soc., Perkin Trans. 2* **1993**, 799.

[33] a) P. Pulay, *Chem. Phys. Lett.* **1980**, *73*, 393; b) P. Pulay, *J. Comput. Chem.* **1982**, *3*, 556.

[34] *Molekel*, Advanced Interactive 3D-Graphics for Molecular Sciences, Swiss National Supercomputing Center. https://ugovaretto.github.io/molekel/

[35] a) L. E. Briand, G. T. Baronetti, H. J. Thomas, *Appl. Catal., A.* **2003**, *256*, 37; b) D. Honda, S. Ikegami, T. Inoue, T. Ozeki, A. Yagasaki, *Inorg. Chem.* **2007**, *46*, 1464; c) Y. Li, E. Wang, S. Wang, Y. Duan, C. Hu, N. Hu, H. Jia, *J. Mol. Struct.* **2002**, *611*, 185; d) C.-M. Liu, D.-Q. Zhang,

D.-B. Zhu, *Cryst. Growth Des.* **2006**, *6*, 524; e) F.-X. Liu, C. Marchal-Roch, D. Dambournet, A. Acker, J. Marrot, F. Sécheresse, *Eur. J. Inorg. Chem.* **2008**, 2191; f) E.-B. Wang, B.-T. Li, Z.-P. Wang, B.-J. Zhang, *Chem. Res. Chin. Univ.* **1996**, *12*, 322.

[36] N. E. Brese, M. O'Keeffe, *Acta Crystallogr. Sect. B* **1991**, *47*, 192.

[37] F.-Q. Zhang, W. Guan, L.-K. Yan, Y.-T. Zhang, M.-T. Xu, E. Hayfron-Benjamin, Z.-M. Su, *Inorg. Chem.* **2011**, *50*, 4967.

[38] R. S. Winter, J. Yan, C. Busche, J. S. Mathieson, A. Prescimone, E. K. Brechin, D.-L. Long, L. Cronin, *Chem. Eur. J.* **2013**, *19*, 2976.

[39] a) H. N. Miras, D.-L. Long, P. Kögerler, L. Cronin, *Dalton Trans.* **2008**, 214; b) E. F. Wilson, H. Abbas, B. J. Dunscombe, C. Streb, D.-L. Long, L. Cronin, *J. Am. Chem. Soc.* **2008**, *130*, 13876.

[40] C. Baffert, S. W. Feldberg, A. M. Bond, D.-L. Long, L. Cronin, *Dalton Trans.* **2007**, 4599.

[41] L.-H. Bi, U. Kortz, M. H. Dickman, S. Nellutla, N. S. Dalal, B. Keita, L. Nadjo, M. Prinz, M. Neumann, *J. Cluster Sci.* **2006**, *17*, 143.

[42] B. Keita, R. Contant, P. Mialane, F. Sécheresse, P. de Oliveira, L. Nadjo, *Electrochem. Commun.* **2006**, *8*, 767.

[43] J. J. Altenau, M. T. Pope, R. A. Prados, H. So, *Inorg. Chem.* **1975**, *14*, 417.

[44] H. So, C. M. Flynn, Jr., M. T. Pope, *J. Inorg. Nucl. Chem.* **1974**, *36*, 329.

[45] S. P. Harmalker, M. A. Leparulo, M. T. Pope, *J. Am. Chem. Soc.* **1983**, *103*, 4286.

[46] R. Kripal, M. Maurya, H. Govind, *Physica B* **2007**, *392*, 281.

[47] A. Aboukaïs, C. Haubtmann, J. J. André, C. Desquilles, M. Dourdin, I. Matthes-Juventin-Andrieu, F. C. Aïssi, M. Guelton, *J. Chem. Soc., Faraday Trans.* **1995**, *91*, 1025.

[48] I. Kaminker, H. Goldberg, R. Neumann, D. Goldfarb, *Chem. Eur. J.* **2010**, *16*, 10014.

[49] a) C. W. Lee, H. So, K. R. Lee, *Bull. Korean Chem. Soc.* **1986**, *7*, 39; b) C. W. Lee, H. So, K. R. Lee, *Bull. Korean Chem. Soc.* **1986**, *7*, 108.

[50] H. N. Miras, D. Stone, D.-L. Long, E. J. L. McInnes, P. Kögerler, L. Cronin, *Inorg. Chem.* **2011**, *50*, 8384.

[51] M. Otake, Y. Komiyama, T. Otaki, *J. Phys. Chem.* **1973**, *77*, 2896.

[52] J. Park, H. So, *Bull. Korean Chem. Soc.* **1994**, *15*, 752.

[53] D. P. Smith, H. So, J. Bender, M. T. Pope, *Inorg. Chem.* **1973**, *12*, 685.

[54] E. Cadot, M. Fournier, A. Tézé, G. Hervé, *Inorg. Chem.* **1996**, *35*, 282.

[55] S. P. Harmalker, M. T. Pope, *J. Am. Chem. Soc.* **1981**, *103*, 7381.

[56] A. Müller, J. Döring, M. I. Khan, V. Wittneben, *Angew. Chem. Int. Ed.* **1991**, *30*, 210.

[57] C. M. Varghese, A. Shunmugasundaram, R. Murugesan, T. Jeyabalan, *Proc. Indian Acad. Sci.* **2002**, *114*, 75.

[58] A.-L. Barra, D. Gatteschi, B. S. Tsukerblat, J. Döring, A. Müller, L.-C. Brunel, *Inorg. Chem.* **1992**, *31*, 5132.

[59] a) W.-M. Bu, L. Ye, G.-Y. Yang, M.-C. Shao, Y.-G. Fan, J.-Q. Xu, *Chem. Commun.* **2000**, 1279; b) M. I. Khan, Y. Chang, Q. Chen, H. Hope, S. Parking, D. P. Goshorn, J. Zubieta, *Angew. Chem. Int. Ed.* **1992**, *31*, 1197; c) L.-S. You, Q.-Y. Zhu, X. Zhang, Y.-Y. Pu, G.-Q. Bian, J. Dai, *Cryst. Eng. Comm.* **2013**, *15*, 2411; d) S. T. Zheng, J. Zhang, G.-Y. Yang, *Eur. J. Inorg. Chem.* **2004**, 2004; e) S.-T. Zheng, J. Zhang, G.-Y. Yang, *Inorg. Chem.* **2005**, *44*, 2426.

[60] P. W. Anderson, P. R. Weiss, *Rev. Mod. Phys.* **1953**, *25*, 269.

[61] A. Abragam, B. Bleaney, *Electron Paramagnetic Resonance of Transition Metal Ions*, Clarendon Press, Oxford, **1970**.

[62] C. J. Ballhausen, H. B. Gray, *Inorg. Chem.* **1962**, *1*, 111.

[63] A. M. Khenkin, P. J. Carl, D. Baute, A. M. Raitsimring, A. V. Astashkin, L. J. W. Shimon, D. Goldfarb, M. Neumann, *Inorg. Chim. Acta* **2006**, *359*, 3072.

[64] K. Wittel, R. Manne, *Theor. Chem. Acc.* **1974**, *33*, 347.

[65] M. T. Pope, *Heteropoly and Isopoly Oxometalates*, Springer-Verlag, Berlin, **1983**.

[66] J. A. Weil, J. R. Bolton, J. E. Wertz, *Electron Paramagnetic Resonance*, Wiley-Interscience, New York, **1994**.

[67] S. K. Misra, J. Sun, *Physica B* **1990**, *162*, 331.

[68] N. S. Hush, *Prog. Inorg. Chem.* **1967**, *8*, 391.

[69] M. M. Mossoba, C. J. O'Connor, M. T. Pope, E. Sinn, G. Hervé, A. Tézé, *J. Am. Chem. Soc.* **1980**, *102*, 6864.

[70] R. A. Prados, P. T. Meiklejohn, M. T. Pope, *J. Am. Chem. Soc.* **1974**, *96*, 1261.

[71] a) X. López, J. M. Maestre, C. Bo, J. M. Poblet, *J. Am. Chem. Soc.* **2001**, *123*, 9571; b) X. López, L. Vilà-Nadal, X. Aparicio-Anglès, J. M. Poblet, *Phys. Procedia* **2010**, *8*, 94; c) X. López, I. A. Weinstock, C. Bo, J. P. Sarasa, J. M. Poblet, *Inorg. Chem.* **2006**, *45*, 6467.